

# A High-Fidelity, Low-Order Propulsion Power Model for Fixed-Wing Electric Unmanned Aircraft

Or D. Dantsker\*, Mirco Theile†, and Marco Caccamo‡

*University of Illinois at Urbana–Champaign, Urbana, IL 61801*

In recent years, we have seen an uptrend in the popularity of UAVs driven by the desire to apply these aircraft to areas such as precision farming, infrastructure and environment monitoring, surveillance, surveying and mapping, search and rescue missions, weather forecasting, and more. These aircraft are more often being fully powered by electric power sources and a major technical hurdle is that of drastically reducing overall power consumption so they can be powered by solar arrays, and for long periods of time. To do so, the power requirement of an aircraft and the conversion efficiency of its propulsion system, from electrical energy to thrust, must be parametrized so that it can be improved. This paper describes a high-fidelity, low-order power model for electric, fixed-wing unmanned aircraft using flight path information. The motivation behind this work is the development of computationally-intensive, long-endurance solar-powered unmanned aircraft, the UIUC Solar Flyer, which will have continuous daylight ability to acquire and process high resolution visible and infrared imagery. Therefore, having an accurate power model will aid in providing the ability to predict power usage for future mission flight segments, which will be vital for energy-conscious path planning. Compared to works in the existing literature, the model presented follows a holistic approach for fixed-wing electric UAV power modeling that encompasses both aircraft aerodynamics and propulsion models under realistic assumptions. The model developed is able to very accurately estimate the power consumption of an electric UAV based on flight path state, without needing precise aerodynamic measurements, therefore doing so with minimal computation power. The propulsion power model was evaluated by means of flight testing as well as simulation and showed errors ranging from negligible to approximately 5%.

## Nomenclature

$L/D$	= lift-to-drag ratio	$P_{motor}$	= motor power
$PWM$	= pulse width modulation	$P_{propulsion}$	= total propulsion power consumption
$UAV$	= unmanned aerial vehicle	$P_{thrust}$	= aerodynamic power from propeller
$\vec{a}$	= aircraft acceleration vector	$P_{ss}$	= steady state power
$b$	= wingspan	$q$	= dynamic pressure
$c$	= wing mean chord	$R$	= internal motor resistance
$C_D$	= drag coefficient	$S$	= wing area
$C_{D_i}, C_{D_o}$	= induced and parasitic drag coefficients	$t_{pwm}$	= throttle percentage based on PWM
$C_L$	= lift coefficient	$T$	= thrust
$CF$	= centrifugal force	$T_{ss}$	= steady state thrust
$D$	= drag	$U_{bat}$	= battery terminal voltage
$\vec{F}$	= force vector	$U_m$	= motor terminal voltage
$g$	= gravitational acceleration	$\vec{v}$	= velocity vector
$i_0$	= zero load motor current	$v$	= velocity
$K$	= aerodynamic constant	$W$	= weight
$K_i, K_p$	= propulsion model constants	$\gamma$	= climb angle
$K_v$	= motor speed constant	$\eta_p$	= propeller efficiency
$L$	= lift force	$\eta_m$	= motor efficiency
$L/D$	= lift-to-drag ratio	$\phi$	= roll (bank) angle
$m$	= aircraft mass	$\Omega$	= shaft rotation rate
$P$	= power	$\rho$	= density of air
$P_{dyn}$	= dynamic power		

\*Ph.D. Student, Department of Aerospace Engineering, AIAA Student Member. dantske1@illinois.edu

†Research Scholar, Department of Computer Science. mircot@illinois.edu

‡Professor, Department of Computer Science. mcaccamo@illinois.edu

## I. Introduction

In recent years, we have seen an uptrend in the popularity of UAVs driven by the desire to apply these aircraft to areas such as precision farming, infrastructure and environment monitoring, surveillance, surveying and mapping, search and rescue missions, weather forecasting, and more. These aircraft are more often being fully powered by electric power sources, including batteries and solar arrays. A major technical hurdle to overcome is that of drastically reducing the overall power consumption of these UAVs so that they can be powered by solar arrays, and do so for long periods of time. In order to do so, the power requirement of an aircraft and the conversion efficiency of its propulsion system, from electrical energy to thrust, must be parametrized so that it can be improved.

This paper describes the development and experimental evaluation of a high-fidelity, low-order power model for electric, fixed-wing unmanned aircraft. The motivation behind this work is the development of computationally-intensive, long-endurance solar-powered unmanned aircraft, the UIUC Solar Flyer.<sup>1,2</sup> The completed 4.0 m (157 in) wingspan aircraft will weight approximately 2.5 kg (88 oz), will be instrumented with a flight control and data acquisition system as well as an embedded core graphics processing unit, and will have continuous daylight ability to acquire and process high resolution visible and infrared imagery. Therefore, having an accurate power model will provide the ability to predict power usage for future mission flight segments, which will be vital for energy-conscious path planning or simulation.<sup>3</sup>

Previous works have separately looked at aircraft power modeling<sup>4–9</sup> and propulsion system modeling<sup>10–14</sup> with varying degrees of assumptions. Compared to works in the existing literature, the propulsion power model presented follows a holistic approach for UAV power modeling that encompasses both aircraft and propulsion models under realistic assumptions using first-order methods. The model uses two types of flight mechanics derivations for the power required, which are based on flight path state, without needing precise in-flight aerodynamic measurements. The results were evaluated by means of flight testing, using a highly accurate data acquisition system, as well as simulation.

This paper will first examine the background and motivation for power modeling. Then an overview of the power model will be given. This will be followed by the development of the power model using first-order motor theory and two types of flight mechanics derivations. Next, an evaluation of the power model through flight testing will be presented and discussed. Finally, a summary and statement of future work will be given.



Figure 1: The UIUC Solar Flyer aircraft flying with a slight bank angle.

## II. Background and Motivation

The traditional approach for small size UAVs is to capture data on the aircraft, stream it to the ground through a high power data-link, process it remotely (potentially off-line), perform analysis, and then relay commands back to the aircraft as needed.<sup>15–18</sup> However, given the finite energy resources found onboard an aircraft (e.g. batteries and solar arrays), the traditional design greatly limits aircraft endurance since significant power is consumed for transmission of visual data instead of being allocated to keeping the aircraft flying. All the mentioned application scenarios would benefit by carrying a high performance embedded computer system to minimize the need for data transmission. Figure 2 shows an estimation for the power consumption break down for a long-endurance UAV with a high performance computational platform onboard.

Thus as mentioned earlier, a major technical hurdle to overcome is that of drastically reducing the overall power consumption of these UAVs so that they can be powered by solar arrays. The process of reducing aircraft power consumption is required to reduce the aircraft weight, prolong flight time, and ultimately reduce cost in order to support the widespread adoption of UAVs for different types of missions. There have been many existing aircraft that use solar panels and are able to sustain flight during all daylight hours, however, lack the ability to perform significant on-board computation beyond automating flight.<sup>19–23</sup> On the other hand, there are several existing aircraft that use solar panels and batteries and are able to perform a variety of on-board tasks;<sup>24,25</sup> however, lack the ability to sustain flight during all daylight hours. Therefore, in order to shift the paradigm of solar powered flight, the UIUC Solar Flyer is being developed with the aim of performing computationally-intensive on-board data processing and do so during all daylight hours.

The UIUC Solar Flyer was designed using a mixture of trade studies and power simulations in order to enable a variety of all-daylight hour missions while minimizing aircraft size. The aircraft is being built from a majority of commercial-off-the-shelf components in order to minimize both development time and cost. The completed 4.0 m (157 in) wingspan UIUC Solar Flyer aircraft will weight approximately 2.5 kg (88 oz) and have continuous daylight ability to acquire and process high resolution visible and infrared imagery. The aircraft will be instrumented with an integrated autopilot and high-fidelity data acquisition system as well as an embedded 256 core graphics processing unit (GPU). The aircraft will be powered by a 65 W gallium arsenide (GaAs) solar array from Alta Devices.<sup>26</sup> The aircraft configuration, sizing, and propulsion system were all chosen based on analysis of estimated solar power production and aircraft, instrumentation, and avionics power consumption.

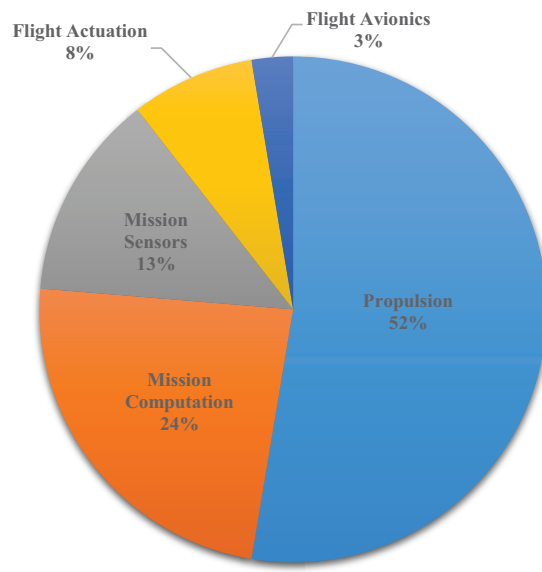


Figure 2: Estimated breakdown of power consumption on computationally intensive UAV based on sizing and experimental data collected.

### III. Overview

On an electric UAV, there are a variety of power-consuming components. The total power consumption of the aircraft can be broken down into categories, as shown in Figure 3, including: propulsion, actuation, flight control sensors, flight control computation, mission sensors, and mission computation. This breakdown follows the estimation presented in Section II. For the purpose of this paper, only propulsion power will be discussed.

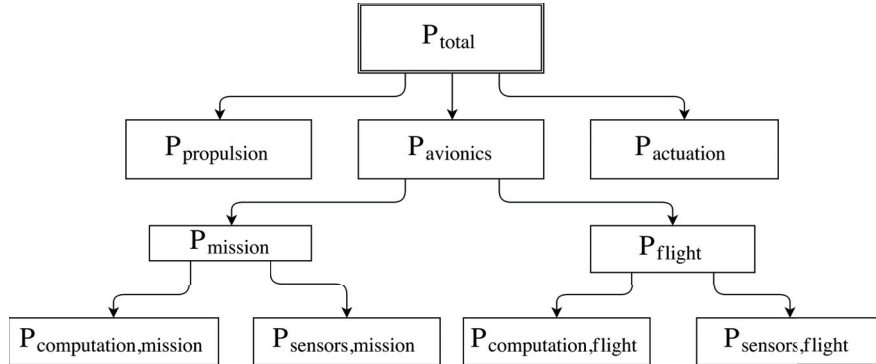


Figure 3: Breakdown of power-consuming components on a fixed-wing electric UAV.

The propulsion power model analytically explains how power transitions from battery power into thrust power. Figure 4 provides a high level diagram of the propulsion power model. From left to right, first, the batteries provide the propulsion power. Then, the motor converts the electric power into rotational power to drive the propeller with an efficiency loss. After that, the propeller converts the rotation power into thrust power applying a forward thrust force to the airplane, also with an efficiency loss. Thus, the product of the propulsion power, motor efficiency, and propeller efficiency is the thrust power:

$$P_{propulsion} \cdot \eta_m \cdot \eta_p = P_{thrust} \quad (1)$$

Therefore, if the thrust power, motor efficiency, and propeller efficiency are known, the propulsion power can be found. The propulsion power model effectively provides this transformation.

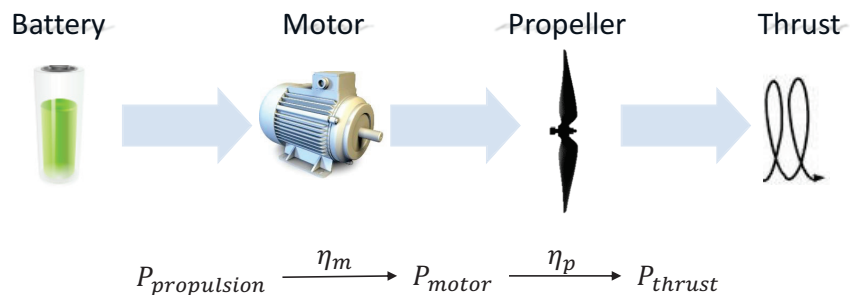


Figure 4: High level diagram of the propulsion power model.

It should be noted that the propulsion power model neglects efficiency losses at the motor electronic speed controller. This decision was made because unlike the motor and propeller, the controller has relatively small and constant losses throughout the operating range it is used in. Additionally, all experimental work currently being done has power measured at the controller and therefore the controller efficiency cannot be measured.

## IV. Model Development

In order to make the power model as versatile as possible, state variable inputs are restricted to easily measurable values. Specifically, the variable inputs are properties of the aircraft maneuver including velocity, acceleration, roll (bank) angle, and climb angle. Doing so makes certain assumptions<sup>a</sup>, which will work well for the overwhelming majority of long-endurance UAV flight. Therefore, the power model provides an estimation based on the motion of the aircraft, i.e. flight path, with minimal knowledge of the aircraft flight mechanics attributes. Figure 5 shows how the model is cascaded from the input variables, through a flight mechanics model, a propeller model, and a motor model. This follows the high-level explanation in the previous section, similar to Equation (1), however in a backwards manner.

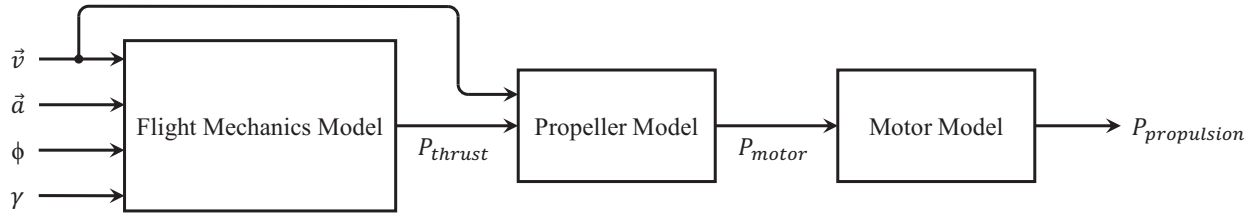


Figure 5: Aircraft propulsion power modeling based on aircraft state.

### A. Flight Mechanics Model

The flight mechanics model takes into account power required for steady-state flight as well as dynamic maneuvers. Specifically, the total thrust power is given by

$$P_{thrust} = P_{ss} + P_{dyn} \quad (2)$$

The steady state power portion of the thrust power,  $P_{ss}$ , is calculated from steady state maneuver data that can be measured or simulated including velocity  $v$ , roll (bank) angle  $\phi$ , and climb angle  $\gamma$ . Figure 6 shows these state variables applied level, turning, and climbing flight<sup>b</sup>. The remainder of the steady state portion of the propulsion power model will be derived from elementary flight mechanics principles<sup>27</sup> in Subsections 1 and 2 using the assumptions of a constant lift-to-drag ratio and a non-constant lift-to-drag ratio, respectively.

The steady state power is only valid for steady-state maneuvers and greatly differ from total thrust power in maneuvers that incorporate acceleration. However, it is still useful in calculating the total thrust power in such maneuvers. To incorporate the dynamics into the power model, dynamics power,  $P_{dyn}$ , is added. The dynamic power is calculated based on Newton's second law

$$\vec{F}(\vec{a}) = m\vec{a} \quad (3)$$

and that power is equal to the dot product of force and velocity,

$$P(\vec{F}, \vec{v}) = \vec{F} \cdot \vec{v} \quad (4)$$

Putting these expressions together gives the dynamic power as

$$P_{dyn}(\vec{a}, \vec{v}) = m(\vec{a} \cdot \vec{v}) \quad (5)$$

It is assumed the effect of rotational accelerations are negligible. Additionally, the model can be extended to take into account constant wind as well as wind gusts by modifying  $\vec{v}$  and  $\vec{a}$  in the previous expressions.

<sup>a</sup>It is assumed that the angle-of-attack and incidence angle sum to zero and thus the flight path climb angle is equal to the measurable pitch angle. Additionally, it is assumed that there is minimal side-slip allowing for the turn radius to be calculated directly from the roll angle.

<sup>b</sup>Note that based on the above stated assumptions, velocity is in the thrust direction.

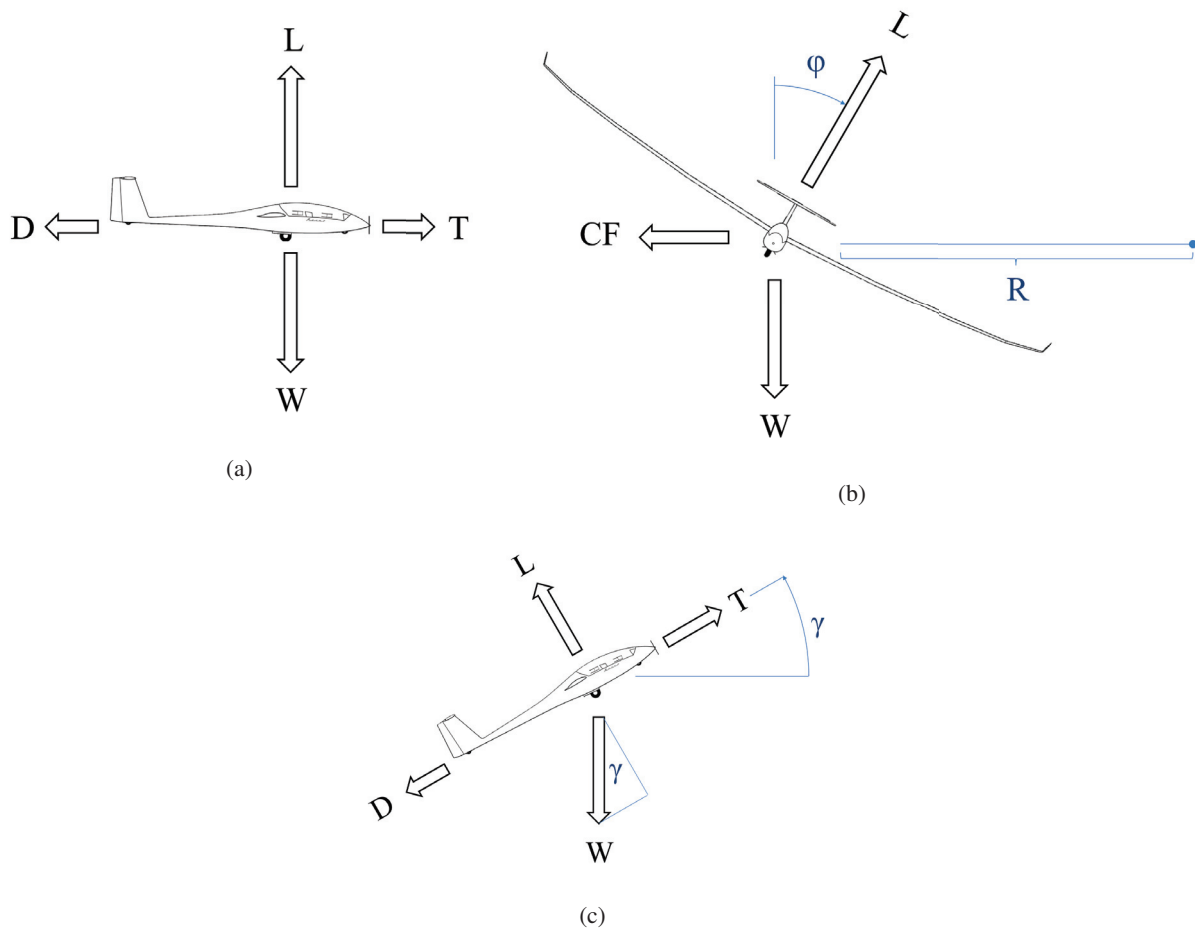


Figure 6: Steady-state forces on an aircraft in (a) level flight, (b) turning flight and (c) climbing flight.

## 1. Constant Lift-to-Drag Ratio Assumption

For steady state flight to occur, there must be an equilibrium of forces and moments. As depicted in Figure 6a, there are four basic forces in level (cruise) flight: lift upward  $L$ , drag backward  $D$ , thrust forward  $T$ , and weight downward  $W$ . As these forces directly and solely oppose each other in equilibrium level flight, the magnitude of lift is equal to that of weight

$$L = W \quad (6)$$

where weight is equal to the aircraft mass multiplied by the gravitational acceleration

$$W = mg \quad (7)$$

And likewise the magnitude of thrust is equal to that of drag,

$$T = D \quad (8)$$

The ratio of the lift force to the drag force, the so called lift-to-drag ratio  $L/D$ , gives a measure of the aircraft design efficiency. In this derivation, it will be assumed that  $L/D$  is approximately constant as the aircraft operates in a relatively small range of angles-of-attack. Thrust is therefore

$$T = \frac{W}{L/D} \quad (9)$$

Per Equation (4), power is the product of thrust and velocity

$$P_{ss}(\vec{v}) = \frac{W \|\vec{v}\|}{L/D} \quad (10)$$

In a level turn, shown in 6b, the airplane is rolled to a desired roll angle,  $\phi$ . Due to the equilibrium of forces, the required lift force needs to be

$$L = \frac{W}{\cos \phi} \quad (11)$$

resulting in the power being

$$P_{ss}(\vec{v}, \phi) = \frac{P_{ss}(\vec{v})}{\cos \phi}. \quad (12)$$

It is important to note that Equation (12) includes the equation for level flight, Equation (10), as it reverts to it, i.e. is equal to  $P_{ss}$ , when  $\phi = 0$  (the aircraft is in level flight).

Similar to the level turn, the steady-state power of the climbing [or descending] flight can also be derived based on the equilibrium of forces. Figure 6c shows the schematics of a climb flight in which the airplane is flying with a climb angle  $\gamma$ . Balancing the forces yields the relation for thrust

$$T = D + W \sin \gamma \quad (13)$$

and the relation for lift

$$L = W \cos \gamma \quad (14)$$

Combining these yields for the steady-state power.

$$P_{ss}(\vec{v}, \gamma) = P_{ss}(\vec{v}) (\cos \gamma + (L/D) \sin \gamma) \quad (15)$$

Similarly, when the climb angle is zero,  $\gamma = 0$ , the equation reverts to that of level flight.

In most cases the two maneuvers are performed separately so that Equations (12) and (15) can be used individually. In some cases, however, both maneuvers are performed at the same time resulting in a spiral flight. As an approximation for the steady-state power, it is assumed that both maneuvers do not influence one another, resulting in this product:

$$P_{ss}(\vec{v}, \phi, \gamma) = \frac{mg \|\vec{v}\|}{L/D} \frac{\cos \gamma + (L/D) \sin \gamma}{\cos \phi} \quad (16)$$

## 2. Non-Constant Lift-to-Drag Ratio Assumption

With the assumption that the lift-to-drag ratio is not constant and that a spiral is made up of a turn and climb that do influence each other, a new approach is needed involving additional information to solve for the steady state propulsion power. Specifically, in order to define the spiral, Equations (11) and (14) are combined as

$$L = W \frac{\cos \gamma}{\cos \phi} \quad (17)$$

and Equation (13) is re-written as

$$D = T - W \sin \gamma \quad (18)$$

The expressions for lift and drag are introduced as

$$L = qSC_L \quad (19)$$

$$D = qSC_D \quad (20)$$

where  $S$  is the reference surface area,  $C_L$  and  $C_D$  are the lift and drag coefficients, respectively, and dynamic pressure  $q$  defined by

$$q = \frac{1}{2}\rho v^2 \quad (21)$$

Here,  $\rho$  is the air density. Therefore, the expressions for the lift coefficient can be re-written as

$$C_L = \frac{2L}{\rho v^2 S} \quad (22)$$

The drag coefficient is defined

$$C_D = C_{D_o} + C_{D_i} \quad (23)$$

where  $C_{D_o}$  is the parasitic drag coefficient at zero lift and  $C_{D_i}$  is the induced drag coefficient. The induced drag is expressed as a function of lift by

$$C_{D_i} = KC_L^2 \quad (24)$$

where  $K$  is a constant aerodynamic coefficient based on the wing platform shape<sup>c</sup>. Inserting Equation (24) into Equation 23 yields

$$C_D = C_{D_o} + KC_L^2 \quad (25)$$

and then inserting Equation (22) yields

$$C_D = C_{D_o} + \frac{4K}{\rho^2 S^2} \frac{L^2}{v^4} \quad (26)$$

Therefore, based on the expression for drag from above

$$D = \frac{1}{2}\rho S C_{D_o} v^2 + \frac{2K}{\rho S} \frac{L^2}{v^2} \quad (27)$$

Inserting Equation (17) yields

$$D = \frac{1}{2}\rho S C_{D_o} v^2 + \frac{2K}{\rho S} \frac{W^2}{v^2} \frac{\cos^2 \gamma}{\cos^2 \phi} \quad (28)$$

And setting the above equation to Equation (18) and inserting Equation (7) for weight gives

$$T = \frac{1}{2}\rho S C_{D_o} v^2 + \frac{2Km^2 g^2}{\rho S} \frac{\cos^2 \gamma}{v^2 \cos^2 \phi} + mg \sin \gamma \quad (29)$$

Per Equation (4), since power is the product of thrust and velocity

$$P_{ss} = \frac{1}{2}\rho S C_{D_o} v^3 + \frac{2Km^2 g^2}{\rho S} \frac{\cos^2 \gamma}{v \cos^2 \phi} + mg v \sin \gamma \quad (30)$$

---

<sup>c</sup> $K = 1/\pi e AR$ , where  $e$  is the Oswald efficiency factor and  $AR$  is the wing aspect ratio.

This expression can be simplified by assigning constants

$$P_{ss} = K_p v^3 + K_i \frac{\cos^2 \gamma}{v \cos^2 \phi} + mgv \sin \gamma \quad (31)$$

where

$$K_p = \frac{1}{2} \rho S C_{D_0} \quad (32)$$

$$K_i = \frac{2Km^2 g^2}{\rho S} \quad (33)$$

It should be noted that these constants can be calculated from aircraft data; however, without pre-existing aircraft performance data, the constants are more easily determined from training data using linear regression.

## B. Propeller and Motor Models

With the calculated thrust power, the motor and propeller efficiency can now be incorporated to calculate the input power needed to produce this thrust. The relation is given by rearranging Equation (1)

$$P_{propulsion} = \frac{P_{thrust}}{\eta_m \cdot \eta_p} \quad (34)$$

where  $\eta_p$  is the propeller efficiency and  $\eta_m$  is the motor efficiency. The problems arising from this equation are that both efficiency factors themselves depend on numerous factors that are directly or indirectly related to thrust and velocity.

### 1. Propeller Efficiency

The propeller efficiency can be derived using blade element momentum theory (BEMT) and sectional airfoil theory as done in.<sup>28</sup> However, BEMT curves are highly sensitive to variation of the parameters used. In order to increase model accuracy, experimental data for propeller performance can be obtained from wind tunnel propeller testing and/or an existing database,<sup>29</sup> with interpolation being done as required.

Figure 7 provides example propeller performance polars for the Aeronaut CAM 13x6.5 propeller, which will be used on the UIUC Solar Flyer.

### 2. Motor Efficiency

The motor efficiency,  $\eta_m$ , for a brushless DC-motor can be calculated analytically using the relation between motor terminal voltage  $U_m$  and shaft rotation rate  $\Omega$  and a variety of fixed motor parameters. A first order approximation<sup>30</sup> is given as

$$\eta_m(\Omega, U_m) = \left( 1 - \frac{i_0 R}{U_m - \Omega/K_v} \right) \frac{\Omega}{U_m K_v} \quad (35)$$

where  $i_0$  as motor current at zero load,  $R$  as motor internal resistance and  $K_v$  as motor speed constant. A second order approximation<sup>31</sup> can be used; however, it requires additional data, which is not easily obtained from motor manufacturers and needs to be measured by the user through benchtop testing.

A brushless DC-motor is typically controlled using a pulse width modulation (PWM). The PWM signals regulates the motor terminal voltage  $U_m$  by effectively scaling down the battery voltage  $U_{bat}$  by the throttle percentage  $t_{pwm}$ . The relationship can be expressed as

$$U_m = t_{pwm} U_{bat}, \quad t_{pwm} \in [0, 1] \quad (36)$$

It should be noted that detailed experiments have shown that motor efficiency remains relatively constant when using the same propeller. This cannot be said about the efficiency of the propeller, which varies highly.

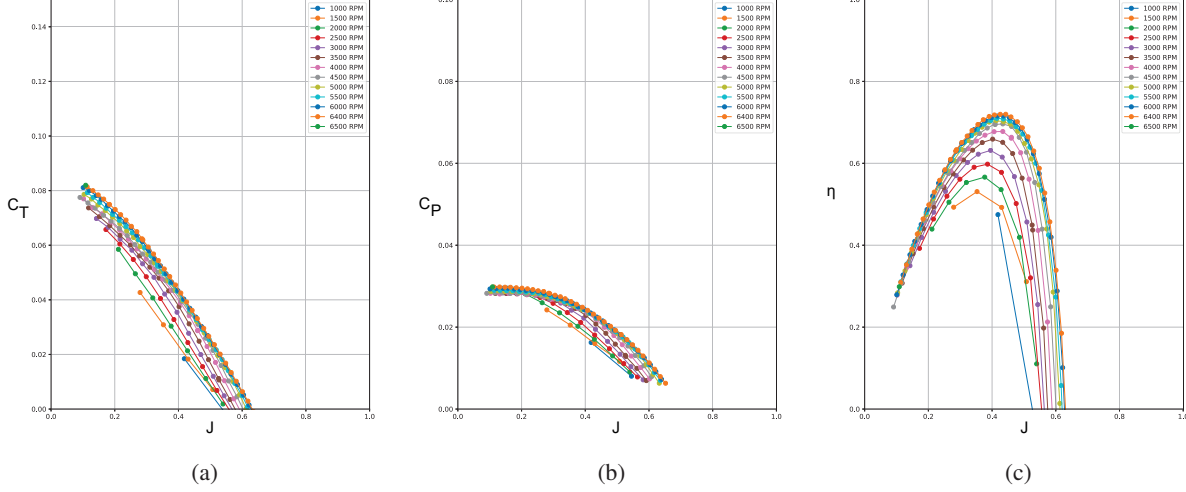


Figure 7: Propeller performance curves for the Aeronaut CAM 13x6.5 propeller: (a) thrust ( $C_T$ ), (b) power ( $C_P$ ), and (c) efficiency ( $\eta$ ) vs. advance ratio ( $J$ )

### C. Complete Propulsion Power Model

Combining the steady state and dynamic thrust power models and propeller and motor models into a generic form yields

$$P_{propulsion}(\vec{v}, \vec{a}, \phi, \gamma) = \frac{P_{ss}(\vec{v}, \phi, \gamma) + P_{dyn}(\vec{v}, \vec{a})}{\eta_p(\vec{v}) \cdot \eta_m} \quad (37)$$

The final expression will vary depending on which form of the steady state thrust power model is used — they are given below.

#### 1. Constant Lift-to-Drag Ratio

$$P_{propulsion} = \frac{mg \|\vec{v}\| \cos \gamma + (L/D) \sin \gamma}{L/D} + m \frac{\vec{a} \cdot \vec{v}}{\eta_p \eta_m \cos \phi} \quad (38)$$

#### 2. Non-Constant Lift-to-Drag Ratio

$$P_{propulsion} = K_p \frac{v^3}{\eta_p \eta_m} + K_i \frac{\cos^2 \gamma}{\eta_p \eta_m v \cos^2 \phi} + mg \frac{v \sin \gamma}{\eta_p \eta_m} + m \frac{\vec{a} \cdot \vec{v}}{\eta_p \eta_m} \quad (39)$$

where  $K_p$  and  $K_i$  were defined earlier.

## V. Evaluation

The propulsion power model was evaluated using the two assumptions through flight testing. An existing aircraft, the Avistar UAV that was previously used for avionics development,<sup>32–34</sup> was flown through a flight path that includes ascends, descends, turns, and cruise flight, and the power measurements were compared to those modeled and simulated.

### A. Aircraft Setup

The Avistar UAV aircraft was developed off of the Great Planes Avistar Elite fixed-wing trainer-type radio control model and has wingspan of 1.59 m and a mass of 3.92 kg. The completed flight-ready aircraft is shown in Figure 8 and its physical specification are given in Table 1. Component specifications can be found in.<sup>33</sup>

The aircraft was instrumented with an AI Volo FC+DAQ flight computer and data acquisition system,<sup>35</sup> which incorporates the open source uavAP autopilot. The specifications of the instrumentation used for flight testing are given in Table 2. Further detail regarding the open source uavAP autopilot can be found in related literature.<sup>2,3</sup>



Figure 8: Flight-ready Avistar UAV used for the evaluation of the power model.

Table 1: Avistar UAV aircraft physical specifications.

Geometric Properties	
<b>Overall Length</b>	1395 mm (55.0 in)
<b>Wing Span</b>	1590 mm (62.5 in)
<b>Wing Area</b>	43.3 dm <sup>2</sup> (672 in <sup>2</sup> )
<b>Aspect Ratio</b>	6.62
Inertial Properties	
Mass/Weight	
<b>Empty (w/o Battery)</b>	3.39 kg (7.46 lb)
<b>4S LiPo Battery</b>	0.53 kg (1.17 lb)
<b>Gross Weight</b>	3.92 kg (8.63 lb)
<b>Wing Loading</b>	90.5 gr/dm <sup>2</sup> (29.6 oz/ft <sup>2</sup> )

Table 2: The instrumentation on the Avistar UAV.

<b>Instrumentation system</b>	AI Volo FC+DAQ 400 Hz system
<b>Sensors</b>	
<b>Inertial</b>	XSens MTi-G-700 AHRS with GPS
<b>Airspeed</b>	AI Volo pitot-static airspeed sensor
<b>Motor Sensors</b>	AI Volo Castle ESC sensor
<b>Power</b>	
<b>Regulator</b>	Built into FDAQ
<b>Battery</b>	Thunder Power ProLite 3S 1350 mAh

## B. Flight Path

The flight path used for evaluation was designed and flown using the uavAP autopilot in an emulation environment, uavEE,<sup>3</sup> and then on the actual aircraft. The experimental results collected during the flight test included aircraft state and power time histories. The resulting flight paths from the experimental flight and the simulated flight in the uavEE are displayed in Figure 9.

The red curve shows the experimental and the green the simulated flight. It can be seen that both flight paths are very similar and only deviate slightly during the turns. These deviations can be explained by disturbances in the real flight caused by light wind gusts. Additionally, it is important to note that the aircraft flown in the emulation environment simulator is a generic radio control trainer with a similar, but not identical, design and performance, and as such, the aircraft aerodynamics and control response will differ.

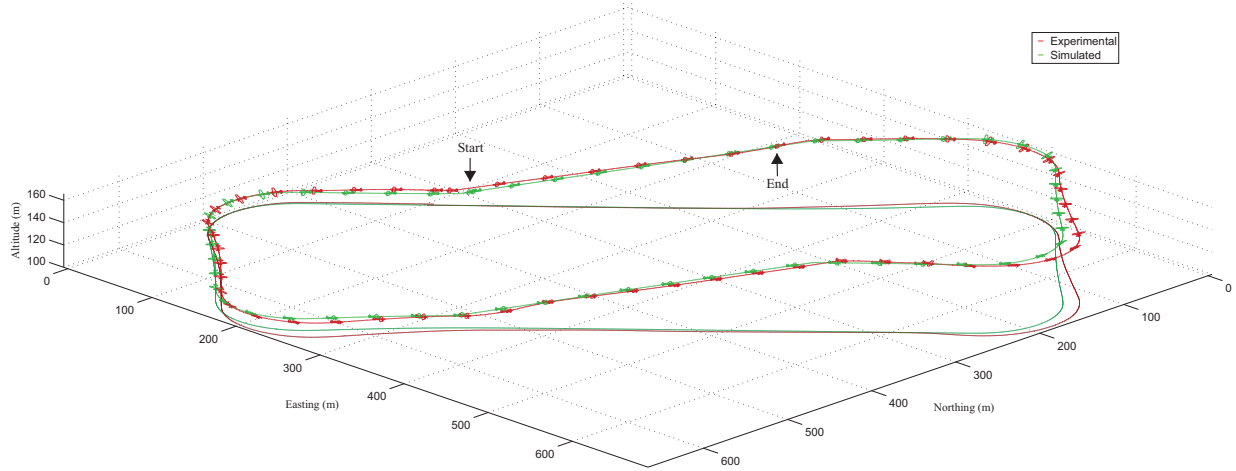


Figure 9: Comparison of aircraft path for experimental (red) and simulated flight (green) results; the airplane is plotted at 6x scale and every 2 seconds.

## C. Propulsion Power Model Evaluation

The power model was evaluated by comparing the power usage as well as the energy consumed for the flight path presented above. The power comparison using the constant lift-to-drag ratio assumption is shown in Figure 10(a) and comparison using the non-constant lift-to-drag ratio assumption is shown in Figure 11(a). Likewise, the energy comparison using the constant lift-to-drag ratio assumption is shown in Figure 10(b) and comparison using the non-constant lift-to-drag ratio assumption is shown in Figure 11(b). The time scale of the power and energy comparison figures relate to the flight path figure with the time 0 s occurring at the flight path "Start" position and the time 100 s occurring at the flight path "End" position.

In these figures, the red "Measured" curves show power and energy from direct measurements collected during the experimental flight. The blue "Modeled" curves show calculated power and energy based on the inertial and GPS state data from the experimental flight. The green "Simulated" curves show calculated power and energy based on the state data from the simulated flight. Following the note in the previous section, that the aircraft simulated is not identical to the aircraft flight tested, large spikes can sometimes be seen in the power figures due to the slightly un-tuned control gains.

## 1. Constant Lift-to-Drag Ratio Assumption

The experimental and model energy curves in Figure 10 show high similarity. There are some areas in Figure 10(a) that have consistently higher or lower power and this correlates to the areas where there is a difference in slope in Figure 10(b). This difference was likely caused by wind coming from the south-west direction during the flight, which either helped or hindered the turns, based on the relative angles, and yielded decreased or increased power consumption, respectively. Otherwise, the two sets of curves were consistent, even including noise. From Figure 10(b), it was estimated that the modeled total consumed propulsion energy was overestimated by approximately 5% with respect to what was measured.

As can be seen in Figure 10(a), the results of the power model that used simulated data does not have the majority of disturbances that the experimental flight has. The spikes in the beginning of the climb are a result from the high accelerations during the pitching maneuver. The simulator pitches faster due to different tuning of the control gains as was mentioned earlier. It is estimated that total consumed propulsion energy is underestimated by approximately 5%.

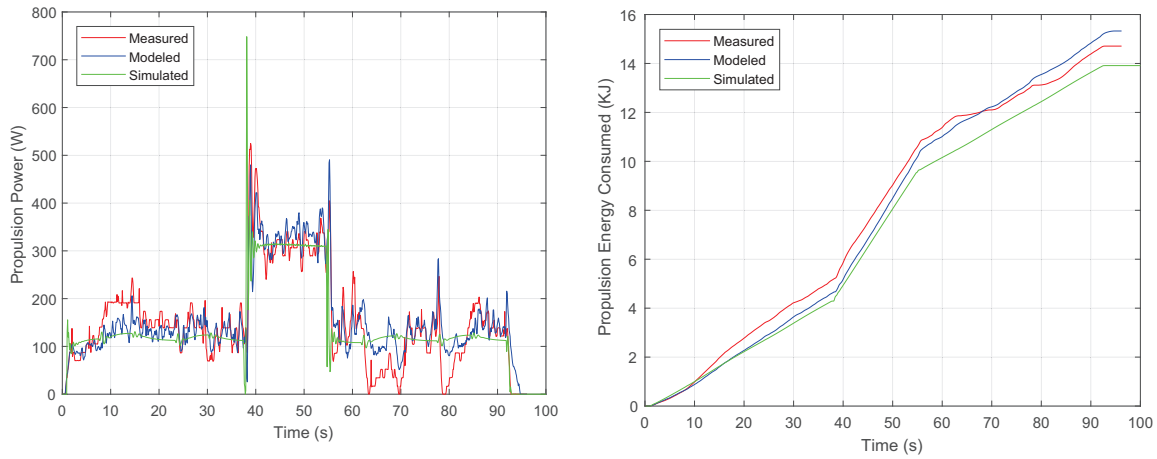


Figure 10: Comparison of (a) propulsion power and (b) energy consumed from experimental measured (red), experimental modeled (blue), and simulated (green) results using the propulsion power model assuming a constant lift-to-drag ratio.

## 2. Non-Constant Lift-to-Drag Ratio Assumption

In order to evaluate the power model using the non-constant lift-to-drag ratio assumption, the constants parameters had to be found using linear regression before it could be used. The regression modeling was performed using two 400 s training flights, with data from shortly after take-off to shortly before landing, to eliminate ground effect disturbances. The resulting modeled and simulated power and energy consumption curves are shown and compared to the measured flight data in Figure 11.

In Figure 11(a) it can be seen that over the trajectory, which contains turns, climbs, descents, and straight lines, the modeled power estimation is nearly identical to the measured power. Figure 11(b) shows that all disturbances during the flight average out and that the power model estimates the consumed energy at the end of the flight almost perfectly.

Similar to the simulated power curve in Figure 10, the simulated power curve in Figure 11 that assumes a non-constant lift-to-drag ratio has a minimal disturbances compared to the experimental power measurements. Additionally, the spikes due to the un-tuned control gains are also present. However, the simulated energy curve in Figure 11(b) differs from the previous figure in that the simulated curve almost overlaps the measured and modeled curves for the majority of the flight path; although, it does somewhat deviate near end of the flight path. Overall, the power model with the non-constant lift-to-drag ratio assumption provides a very good estimation for the energy consumed.

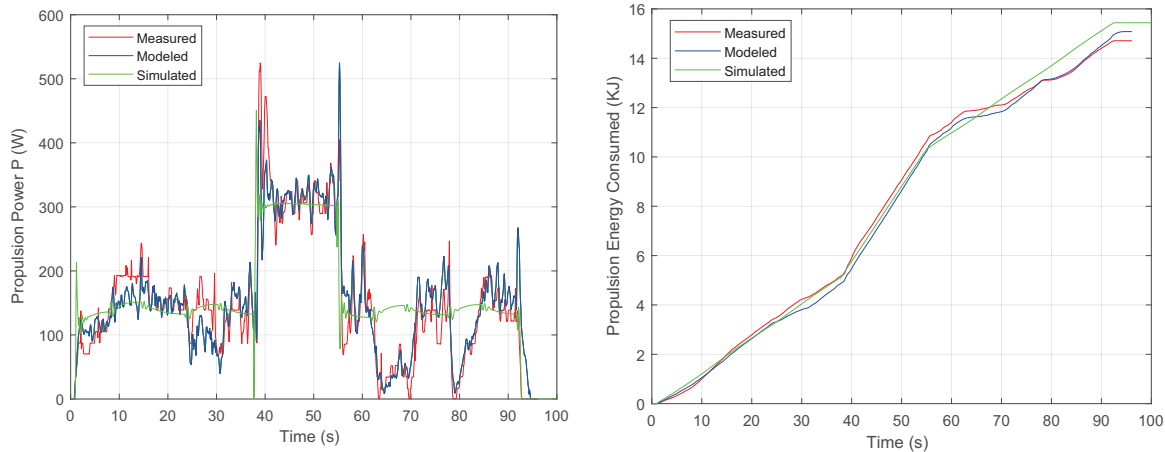


Figure 11: Comparison of (a) propulsion power and (b) energy consumed from experimental measured (red), experimental modeled (blue), and simulated (green) results using the propulsion power model assuming a non-constant lift-to-drag ratio.

## VI. Conclusions

This paper presented a high-fidelity, low-order power model for electric, fixed-wing unmanned aircraft. The power model was developed using both propulsion system modeling of the propeller and motor as well as aircraft power modeling using two types of flight mechanics derivations, with and without assuming a constant lift-to-drag ratio. Compared to existing works, the propulsion power model developed in this paper provides a more holistic approach to UAV propulsion power modeling.

The resulting power model was evaluated by means of flight testing using a highly accurate data acquisition and autopilot system. By flying a reference flight path, which contained turns, climbs, descents, and straight line segments, the flight testing showed very close agreement between the power and energy estimates determined using the power model from aircraft state data and actual experimental power and energy measurements. The power model that used the constant lift-to-drag ratio assumption had an error of approximately 5% while the model that made the non-constant assumption had almost no error.

Using an emulation environment, the reference flight path was also flown using the same autopilot and a simulated radio control model aircraft trainer, which was very similar to the one used in experimental flight testing. The flight path was nearly identical with the exception of 2 corners, where in experimental flight testing, light wind gusts deviated the aircraft slightly. The power and energy data generated was also in close agreement with the experimental data - also within approximately 5%. The significance of this result is that the propulsion power model that was developed is able to very accurately estimate the power consumption of an electric UAV based on flight path state, without needing precise aerodynamic measurements, e.g. angle-of-attack. Therefore power estimation can be done with minimal computation.

## VII. Future Work

The propulsion power model will be expanded in the future to take into account environmental factors such as wind. More flight testing is also planned for evaluating the model over longer periods of time. Additionally, the power model will also be evaluated on other aircraft such as the high aspect ratio UIUC Solar Flyer. Effort will be allocated to optimize the propulsion power model with respect to minimizing computational resources required for estimation, with particular emphasis towards propeller modeling, which currently requires look-up tables.

The propulsion power model will also be integrated into the flight control software running on the UIUC Solar Flyer. Doing so will allow for high-fidelity, low-computation power estimates of current and future power consumption, which is crucial for run-time path planning. Accurate estimates of power consumption will be vital to the flight software to better balance solar power allocation between components, especially the propulsion system and the on-board mission computation platform. Similarly, the power model can also be integrated into pre-flight mission design software.

## Acknowledgments

The material presented in this paper is based upon work supported by the National Science Foundation (NSF) under grant number CNS-1646383. Any opinions, findings, and conclusions or recommendations expressed in this publication are those of the authors and do not necessarily reflect the views of the NSF.

The authors would like to thank Al Volo LLC for their generous loan of data acquisition equipment.

## References

- <sup>1</sup>Dantsker, O. D., Theile, M., Caccamo, M., and Mancuso, R., "Design, Development, and Initial Testing of a Computationally-Intensive, Long-Endurance Solar-Powered Unmanned Aircraft," AIAA Paper 2018-4217, AIAA Applied Aerodynamics Conference, Atlanta, Georgia, June 2018.
- <sup>2</sup>Real Time and Embedded System Laboratory, University of Illinois at Urbana-Champaign, "Solar-Powered Long-Endurance UAV for Real-Time Onboard Data Processing," <http://rtsl-edge.cs.illinois.edu/UAV/>, Accessed Jan. 2018.
- <sup>3</sup>Theile, M., Dantsker, O. D., Nai, R., and Caccamo, M., "uavEE: A Modular, Power-Aware Emulation Environment for Rapid Prototyping and Testing of UAVs," IEEE International Conference on Embedded and Real-Time Computing Systems and Applications, Hakodate, Japan, Aug. 2018.
- <sup>4</sup>Lee, J. S. and Yu, K. H., "Optimal Path Planning of Solar-Powered UAV Using Gravitational Potential Energy," *IEEE Transactions on Aerospace and Electronic Systems*, Vol. 53, No. 3, June 2017, pp. 1442–1451.
- <sup>5</sup>Grano-Romero, C., Garcaa-Juarez, M., Guerrero-Castellanos, J. F., Guerrero-Sanchez, W. F., Ambrosio-Lazaro, R. C., and Mino-Aguilar, G., "Modeling and control of a fixed-wing UAV powered by solar energy: An electric array reconfiguration approach," *2016 13th International Conference on Power Electronics (CIEP)*, June 2016, pp. 52–57.
- <sup>6</sup>Gao, X.-Z., Hou, Z.-X., Guo, Z., Liu, J.-X., and Chen, X.-Q., "Energy management strategy for solar-powered high-altitude long-endurance aircraft," *Energy Conversion and Management*, Vol. 70, No. Supplement C, 2013, pp. 20 – 30.
- <sup>7</sup>Hosseini, S., Dai, R., and Mesbahi, M., "Optimal path planning and power allocation for a long endurance solar-powered UAV," *2013 American Control Conference*, June 2013, pp. 2588–2593.
- <sup>8</sup>Lee, B., Park, P., Kim, C., Yang, S., and Ahn, S., "Power managements of a hybrid electric propulsion system for UAVs," *Journal of Mechanical Science and Technology*, Vol. 26, No. 8, Aug 2012, pp. 2291–2299.
- <sup>9</sup>Ostler, J. and Bowman, W., "Flight Testing of Small, Electric Powered Unmanned Aerial Vehicles," U.S. Air Force T&E Days Conferences, American Institute of Aeronautics and Astronautics, Dec 2005, 0.
- <sup>10</sup>Karabetsky, D., "Solar rechargeable airplane: Power system optimization," *2016 4th International Conference on Methods and Systems of Navigation and Motion Control (MSNMC)*, Oct 2016, pp. 218–220.
- <sup>11</sup>Park, H. B., Lee, J. S., and Yu, K. H., "Flight evaluation of solar powered unmanned flying vehicle using ground testbed," *2015 15th International Conference on Control, Automation and Systems (ICCAS)*, Oct 2015, pp. 871–874.
- <sup>12</sup>Lindahl, P., Moog, E., and Shaw, S. R., "Simulation, Design, and Validation of an UAV SOFC Propulsion System," *IEEE Transactions on Aerospace and Electronic Systems*, Vol. 48, No. 3, JULY 2012, pp. 2582–2593.
- <sup>13</sup>Bradt, J. B. and Selig, M. S., "Propeller Performance Data at Low Reynolds Numbers," *AIAA Aerospace Sciences Meeting, Orlando, Florida, Jan. 2011*.
- <sup>14</sup>Shiau, J. K., Ma, D. M., Chiu, C. W., and Shie, J. R., "Optimal Sizing and Cruise Speed Determination for a Solar-Powered Airplane," *AIAA Journal of Aircraft*, Vol. 47, No. 2, Mar 2010, pp. 622–629.
- <sup>15</sup>Altavian, "Products - Altavian," <http://www.altavian.com/Products>, Accessed Apr. 2015.
- <sup>16</sup>Precision Hawk, "Precision Agriculture, Commercial UAV and Farm Drones For Sale," <http://precisionhawk.com/>, Accessed Apr. 2015.
- <sup>17</sup>MicroPilot, "MicroPilot - MP-Vision," <http://www.micropilot.com/products-mp-visione.htm>, Accessed Apr. 2015.
- <sup>18</sup>Trigger Composites, "Pteryx UAV," <http://www.trigger.pl/pteryx/index.php>, Accessed Apr. 2015.
- <sup>19</sup>Ahn, I.-Y., Bae, J.-S., Park, S., and Yang, Y.-M., "Development and Flight Test of a Small Solar Powered UAV," Vol. 41, 11 2013.
- <sup>20</sup>ETH Zurich's Autonomous Systems Lab, "Atlantik-Solar," <http://www.atlantiksolar.ethz.ch/>, Accessed Apr. 2015.
- <sup>21</sup>Weider, A., Levy, H., Regev, I., Ankri, L., Goldenberg, T., Ehrlich, Y., Vladimirsky, A., Yosef, Z., and Cohen, M., "SunSailor: Solar Powered UAV," <http://webee.technion.ac.il/people/maxcohen/SunSailorArt19nov06.pdf>, Nov. 2006.
- <sup>22</sup>Morton, S., D'Sa, R., and Papanikopoulos, N., "Solar powered UAV: Design and experiments," *2015 IEEE/RSJ International Conference on Intelligent Robots and Systems (IROS)*, 2015, pp. 2460–2466.
- <sup>23</sup>Betancourt, N. J. P., Villamarin, J. E. P., Rios, J. J. V., Bravo-Mosquera, P. D., and Ceron-Munoz, H. D., "Design and Manufacture of a Solar-Powered Unmanned Aerial Vehicle for Civilian Surveillance Missions," *Journal of Aerospace Technology and Management*, Vol. 8, 12 2016, pp. 385 – 396.
- <sup>24</sup>Silent Falcon UAS Technologies, "Silent-Falcon sUAS," <http://www.silentfalconuas.com/Silent-Falcon.html>, Accessed Apr. 2015.
- <sup>25</sup>AeroVironment, "AeroVironment Solar-Powered Puma AE Small Unmanned Aircraft Achieves Continuous Flight for More Than Nine Hours," <http://www.avinc.com/resources/press-release/aerovironment-solar-powered-puma-ae-small-unmanned-aircraft-achieves-contin>, Accessed Apr. 2015.
- <sup>26</sup>Alta Devices, "Technology Brief - Single Junction," <https://www.altadevices.com/wp-content/uploads/2018/01/tb-single-junction-1712-001.pdf>, Accessed Apr. 2018.
- <sup>27</sup>McCormick, B. W., *Aerodynamics, Aeronautics, and Flight Mechanics*, Wiley, 1994.
- <sup>28</sup>Ol, M., Zeune, C., and Logan, M., "Analytical/Experimental Comparison for Small Electric Unmanned Air Vehicle Propellers," *26th AIAA Applied Aerodynamics Conference*, American Institute of Aeronautics and Astronautics, Reston, Virginia, 8 2008.
- <sup>29</sup>UIUC Applied Aerodynamics Group, "UIUC Propeller Data Site," <http://m.selig.ae.illinois.edu/props/propDB.html>.
- <sup>30</sup>Drela, M., "First-Order DC Electric Motor Model," <http://web.mit.edu/drela/Public/web/qprop/motor1theory.pdf>.

<sup>31</sup>Drela, M., "Second-Order DC Electric Motor Model," <http://web.mit.edu/drela/Public/web/qprop/motor2theory.pdf>.

<sup>32</sup>Mancuso, R., Dantsker, O. D., Caccamo, M., and Selig, M. S., "A Low-Power Architecture for High Frequency Sensor Acquisition in Many-DOF UAVs," Submitted to International Conference on Cyber-Physical Systems, Berlin, Germany, April 2014.

<sup>33</sup>Dantsker, O. D., Mancuso, R., Selig, M. S., and Caccamo, M., "High-Frequency Sensor Data Acquisition System (SDAC) for Flight Control and Aerodynamic Data Collection Research on Small to Mid-Sized UAVs," AIAA Paper 2014-2565, AIAA Applied Aerodynamics Conference, Atlanta, Georgia, June 2014.

<sup>34</sup>Dantsker, O. D., Loius, A. V., Mancuso, R., Caccamo, M., and Selig, M. S., "SDAC-UAS: A Sensor Data Acquisition Unmanned Aerial System for Flight Control and Aerodynamic Data Collection," *AIAA Infotech@Aerospace Conference, Kissimmee, Florida, Jan 2015..*

<sup>35</sup>Al Volo LLC, "Al Volo: Flight Systems," <http://www.alvolo.us>.